

An Encapsulated Water Governs Catalysis in a Supramolecular Capsule for Reductive Elimination Reaction from Gold

Valerie Vaissier Welborn^{1,2,3} and Teresa Head-Gordon^{1-5*}

¹Kenneth S. Pitzer Center for Theoretical Chemistry

²Department of Chemistry, University of California, Berkeley

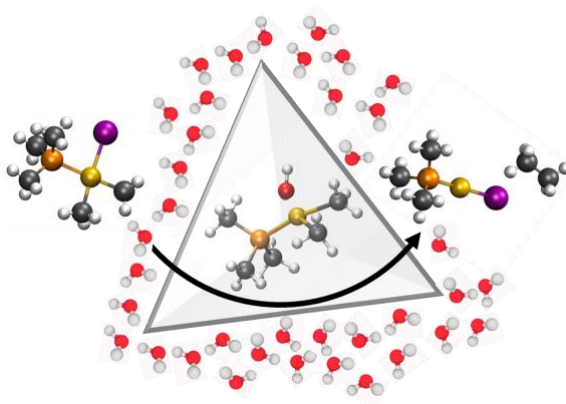
³Chemical Sciences Division, Lawrence Berkeley National Labs, Berkeley

⁴Department of Chemical and Biomolecular Engineering and

⁵Department of Bioengineering, University of California, Berkeley

E-mail: thg@berkeley.edu

Supramolecular assemblies have gained tremendous attention due to their apparent ability to catalyze reactions with the efficiencies of natural enzymes. Using Born-Oppenheimer molecular dynamics and density functional theory, we identify the origin of the catalytic power of the supramolecular assembly $\text{Ga}_4\text{L}_6^{12-}$ on the reductive elimination reaction from gold complexes. By comparing the catalyzed and uncatalyzed reaction in explicit solvent to identify the reaction free energies of the reactants, transition states, and products, we determine that the catalysis arises from an encapsulation of a catalytic moiety- a primary water molecule – that is unlike the biomimetic scenario of catalysis through direct host-guest interactions.



Inspired by the ultimate enzyme catalyst^{1, 2}, supramolecular catalytic systems seek to be biomimetic^{3, 4, 5} for features such as presence of an active site⁶ with optimized non-covalent interactions with the substrate,⁷ electrostatic preorganization that eliminates the reorganization cost paid by the uncatalyzed reaction,^{8, 9} as well as desolvation and dynamical effects that are relevant for the complete catalytic cycle.^{10, 11, 12} In turn, the weak intermolecular interactions that govern supramolecular assemblies offer the undeniable advantage of easy functionalization, reversibility, and fast self-assembly^{5, 13, 14} that overcome limitations of a delicate and more difficult redesign of an enzyme scaffold¹⁵. Supramolecular catalysts have the potential to revolutionize the chemical industry by allowing simpler and more flexible reaction pathways that offers lower cost, reduces the creation of undesired byproducts^{16, 17, 18, 19}, operates in a broad range of conditions.^{20, 21}, and is compatible with renewable and sustainable man-made chemistry.^{22, 23}

Nanocapsule or cage-like supramolecular catalysts have attracted a lot of attention due to their perceived similarities to enzymes and their remarkable efficiencies.^{3, 10, 11, 19, 24} There are two types of nanocage supramolecular systems that (i) encapsulate a catalytic moiety, thereby shielding the reaction from undesired bulk side reactions²⁵ and (ii) only encapsulate reactants and rely on host-guest interactions to promote the reaction as do enzymes. The most notable examples of the latter are the metal-ligand assemblies M_6L_4 introduced by Fujita et al^{4, 26, 27} which can tune the Diels Alder reaction towards the formation of new products, and the M_4L_6 assembly introduced by Raymond and co-workers (Figure 1, top), that catalyzes a number of reactions including Nazarov cyclization of dienol substrates as well as aza-cope rearrangements of cationic enammoniums, with enzymatic efficiencies.^{4, 28, 29, 30, 31}

Relevant to this work, $Ga_4L_6^{12-}$ has been proven to accelerate the alkyl-alkyl reductive elimination from gold(III) complexes by five order of magnitude.^{32, 33} Subsequent experimental studies have revealed that the nanocage catalyzed reaction obeys Michaelis-Menten kinetics, and demonstrating that the $Ga_4L_6^{12-}$ capsule creates a microenvironment that preferentially binds a cationic intermediate as the substrate (Figure 1, bottom).^{32, 34} Our group has shown that the total activation energy of the reaction from this cationic intermediate is lowered by the electrostatic environment emanating from the $Ga_4L_6^{12-}$ system relative to that of a $Si_4L_6^{8-}$ capsule, which is consistent with catalytic trends observed experimentally.³⁵ These results suggest that the catalytic

power of $\text{Ga}_4\text{L}_6^{12-}$ is dominated by the *electrostatics* in favor of a yet to be discovered host-guest mechanism that drives the catalytic effect.

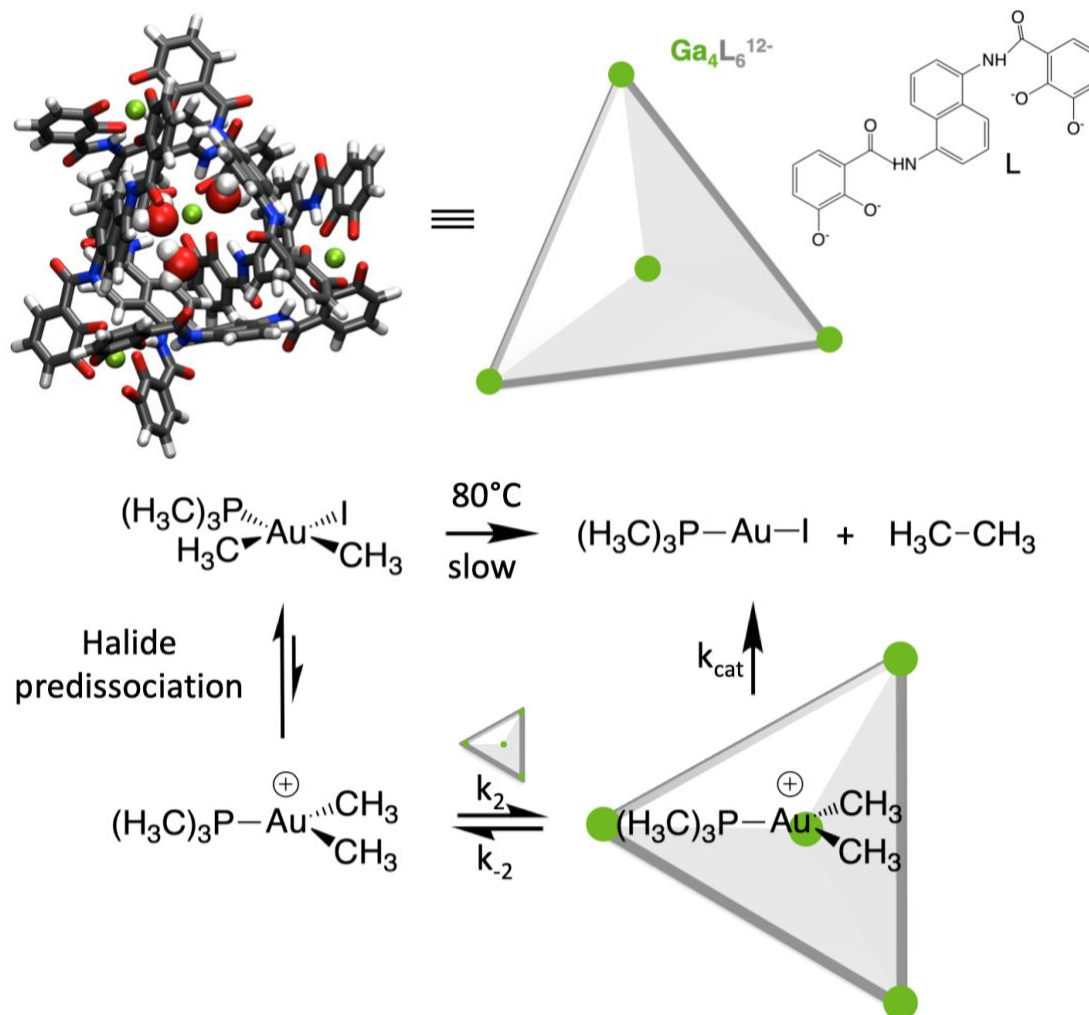


Figure 1. Supramolecular catalyst $\text{Ga}_4\text{L}_6^{12-}$ for the alkyl-alkyl reductive elimination from gold(III) complexes examined in this study. (Top) The $\text{Ga}_4\text{L}_6^{12-}$ ($\text{L}=\text{N},\text{N}'$ -bis(2,3-dihydroxybenzoyl)-1,5-diaminonaphthalene) tetrahedral assembly. (bottom) The uncatalyzed reductive elimination is from trialkylphosphine(dimethyl)gold iodine ($\text{P}(\text{CH}_3)_3(\text{CH}_3)_2\text{AuI}$), whereas the reaction occurring in the nanocage binds the positively charged intermediate $\text{P}(\text{CH}_3)_3(\text{CH}_3)_2\text{Au}^+$ that results from the iodine dissociation of the original complex as proposed in Ref³².

Here we seek to quantify the reaction mechanism of the $\text{Ga}_4\text{L}_6^{12-}$ catalyzed alkyl-alkyl reductive elimination using *ab initio* molecular dynamics (AIMD) of the nanocage in explicit water solvent in order to analyze the electric field interactions responsible for the catalytic acceleration, and to quantify the corresponding electrostatic free energy with respect to the uncatalyzed reaction in water. We find that the $\text{Ga}_4\text{L}_6^{12-}$ nanocapsule is not in fact biomimetic of

an enzyme active site governed by host-guest interactions but rather that the nanocage creates a catalytic moiety- a primary water molecule- that catalyzes the reaction. Although encapsulated water has been shown experimentally to influence the $\text{Ga}_4\text{L}_6^{12-}$ nanocage's ability to catalyze acid-, base- and water-mediated proton transfer³⁰, the role of water has not been elucidated for reactions that do not involve proton transfer. Here we demonstrate that the individual water molecule, encapsulated with a cationic guest, drives the catalytic power of $\text{Ga}_4\text{L}_6^{12-}$ for carbon-carbon reductive elimination from gold.

To rationalize the role of the nanocage construct on the evolution of the reductive elimination, we compare the reaction path of both the catalyzed and uncatalyzed reactions using *ab initio* metadynamics and a frozen string method to determine reactants, products, and transition states, as detailed in Methods. To accelerate the exploration of the free energy landscape, we picked two coordinates as collective variables and calculate the free energy pathway in the reduced two-dimensional space. In this study, our choice of (i) the distance between the carbon atoms of the leaving methyl groups (methyl-methyl distance) and (ii) the coordination number between the leaving carbons and the gold was found to yield a correct transition state ensemble as subsequently confirmed with a committor analysis using unconstrained AIMD trajectories in the complete higher dimensional space of the reaction (see Methods).

In Figure 2, we show the free energy landscapes along the two relevant variables for the uncatalyzed (left) and $\text{Ga}_4\text{L}_6^{12-}$ catalyzed reaction (right). We observe well-defined free energy basins for both the reactant state (RS at 3.0 Å, 0.50) and the product state (PS at 1.5 Å, 0.00). The minimum free energy path connecting RS to PS computed using a frozen string method is depicted by a black dotted line. The transition state on both paths, marked by the gray dotted lines in Figure 2, was found at (2.3 Å, 0.24) for the uncatalyzed and (2.1 Å, 0.36) for the catalyzed reaction. This means that the transition state geometry for the catalyzed reaction is more highly coordinated, with a shorter methyl-methyl distance, consistent with a more restricted environment within the cage. The free energy barrier calculated from these minimum energy paths is 37 and 33 kcal/mol (with and without iodine (Figure S1), respectively) for the uncatalyzed reaction and 24 kcal/mol for the catalyzed reaction. Using a simple transition state theory relationship, $\exp(\Delta G^\ddagger/k_bT)$, this would correspond to a rate acceleration of 3.3×10^7 , in

reasonable agreement with 5.0×10^5 to 2.5×10^6 (depending on halogen ligand) that was determined experimentally²⁹ for this same reactant and reaction.

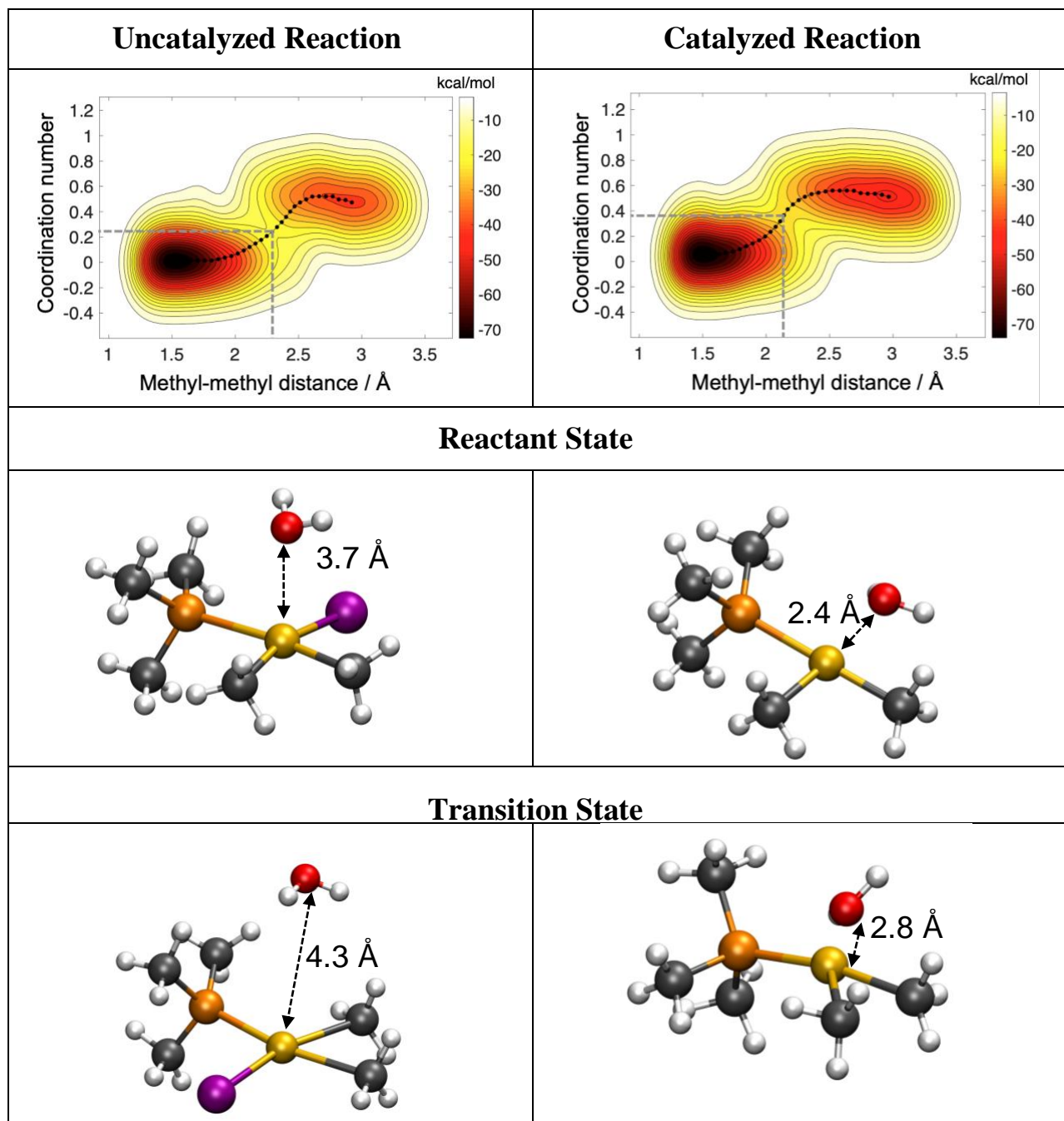


Figure 2. Free energy landscape obtained from *ab initio* metadynamics. The uncatalyzed reaction on the left describes the evolution of the halogenated compound $\text{P}(\text{CH}_3)_3(\text{CH}_3)_2\text{AuI}$ in water. The catalyzed reaction on the right describes the evolution of the encapsulated cation $\text{P}(\text{CH}_3)_3(\text{CH}_3)_2\text{Au}^+$ in water. As an additional reference, we provide in Supporting Information the landscape for the cation $\text{P}(\text{CH}_3)_3(\text{CH}_3)_2\text{Au}^+$ in water in the absence of the cage (Figure S1).

To better understand how the $\text{Ga}_4\text{L}_6^{12-}$ nanocage provides a ~ 9 kcal/mol reduction in the activation energy barrier, we selected snapshots characteristic of the reactant and transition states from the AIMD trajectory, and representative structures are also shown in Figure 2. In the bulk, the closest water molecule is 4 Å away from the gold, likely due to steric and electrostatic constraints emanating from the halogen atom. But in the presence of the cage, two to three water molecules are encapsulated with the reactants, and one of these water molecules is complexed to the gold transition metal. Further analysis reveals that this complexed water remains in close proximity to the encapsulated substrate in the reactant state, whereas the closest water in bulk solution is more labile (Figure S2).

In recent work, our group has analyzed the electrostatic environment of enzyme active sites to show they create large electric fields that are well-aligned with reactive bonds, and act as an important contributor to transition state stabilization as well as reactant state destabilization.^{1, 2} Therefore we calculated the electric fields from different system components, and their contributions to the activation energy barrier, to quantify the catalytic role of the nanocage and encapsulated water molecule vs. that of the greater bulk water environment of the uncatalyzed reaction. We find that the closest water molecule in the bulk does not contribute much to the electric field in the uncatalyzed reaction due to the greater distance and fluctuations that result in poor projections onto the reactive bonds (all fields are less than 5MV/cm in absolute magnitude). For the catalyzed reaction however, the complexed water is stabilized in a position so that it plays a much more important role, with electric field contribution that are bigger than the cage itself.

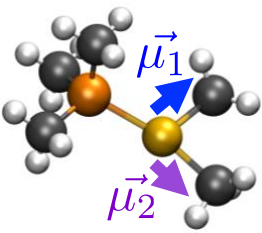
To further quantify the effect of these electric fields on the stabilization of the transition state, we estimated the electrostatic free energy of stabilization of the transition state, $\overline{\Delta G^{elec}}$, defined as follows:

$$\overline{\Delta G^{elec}} = \sum_i -0.048(\vec{\mu}_{TS}^i \cdot \vec{E}_{TS}^i - \vec{\mu}_{RS}^i \cdot \vec{E}_{RS}^i) \quad (1)$$

where the summation is over the number of reactive bonds considered, $\vec{\mu}_X^i$ is the bond dipole moment and \vec{E}_X^i the electric field in state X. Since both the magnitude and the orientation of electric fields are of importance, we projected the fields onto the two bonds that change the most during the reaction, identified as the two gold-methyl bonds as shown in Table 1. When comparing the catalyzed to uncatalyzed reaction, we see that the nanocage environment supports

the overall stabilization of the transition state. However, a large part of this stabilization (~12 kcal/mol) comes from the complexed water encapsulated with the reactants in the cage. The cage itself, although producing large electric fields consistent with its high negative charge, does not contribute much to the free energies. This would suggest that the reductive elimination from gold complexes is in fact catalyzed by a catalytic moiety, a water molecule, that is sequestered from the bulk. In this context, the role of the nanocage is to generate a micro-environment in which this phenomenon is possible, which contrasts from previous speculations that put forward host-guest interactions as the main catalytic process.

Table 1: *Electric fields and corresponding free energies projected onto the two bonds that break during the reaction.* The electric fields are given by the contribution from bulk water, a vicinal water, and from the nanocage for the reactant and transition state of the uncatalyzed and catalyzed reaction. Positive fields are defined in the opposite direction of the flow of electrons. The bond dipoles were computed from the partial charges on the gold and carbon atoms, and using the bond length $d_{\text{Au-Ci}}$ as shown in Figure S3 and Table S1. The unit conversion factor for free energy from the projected electric field on the bond dipole in kcal/mol is 0.048.

		E ₁ / MV/cm			E ₂ / MV/cm			
		Bulk Water	Complexed water	Cage	Bulk water	Complexed water	Cage	
RS	Uncatalyzed reaction	7.54	1.89	N/A	-8.52	-3.40	N/A	
	Catalyzed reaction	-6.72	40.81	-0.21	-6.87	-7.97	-14.13	
TS	Uncatalyzed reaction	22.24	0.09	N/A	35.98	-4.90	N/A	
	Catalyzed reaction	-51.63	19.30	27.27	-31.37	22.27	9.95	
		$\Delta G^\ddagger = - \sum_i (\vec{\mu}_{TS}^i \cdot \vec{E}_{TS}^i - \vec{\mu}_{RS}^i \cdot \vec{E}_{RS}^i)$						
		$\vec{\mu}_{RS}^1$	$\vec{\mu}_{RS}^2$	$\vec{\mu}_{TS}^1$	$\vec{\mu}_{TS}^2$	Bulk water	Complexed water	Cage
Uncatalyzed reaction		-3.96	1.65	-3.37	1.24	-0.65	-0.32	N/A
Catalyzed reaction		-6.15	-2.83	2.05	0.71	9.02	-13.62	-1.04

However, the nanocage does play an implicit role for catalysis since the unhalogenated gold complex compared to the halogenated form will have influence on the charges of the atoms and therefore the bond dipoles, and also since the transition state structure is different in the nanocage when compared to the bulk, and both effects contribute to differences in the bond

dipoles. In other words, the nanocage increases the system's sensitivity to the electric fields, although the true catalytic effect comes from the isolated water molecule(s) within the cage.

In conclusion, the simulations presented in this paper provide new insights into the catalytic power of the cage-like supramolecular catalyst $\text{Ga}_4\text{L}_6^{12-}$. For the alkyl-alkyl reductive elimination from gold(III) complexes, we show here that the two traditional categories to explain their catalytic prowess - i.e. cage-like compounds that encapsulate a catalytic moiety and the ones that use host-guest mechanisms - are actually not so easily separable. We have shown that the $\text{Ga}_4\text{L}_6^{12-}$ nanocage not only encapsulates the reactants but also hosts additional water molecules, of which one complexed guest water serves as the primary catalytic player. At the same time the nanocage host stabilizes the catalytic reactant through loss of a halogen ligand, and preconditions the transition state for greater sensitivity to electric field projections onto the breaking carbon bonds to complete the reductive elimination reaction.

METHODS

All calculations presented in this paper (geometry optimization, molecular dynamics, metadynamics, energy calculations) were performed with Density Functional Theory (DFT) using the dispersion corrected meta-generalized gradient approximation (GGA) functional B97M-V^{36, 37} in combination with a DZVP basis set optimized for multigrid integration³⁸ as implemented in the CP2K software package.^{39, 40} In all cases, we used periodic boundary conditions, 5 grids and a cutoff of 400 Ry.

Starting geometries. The starting geometry for the catalyzed reaction is the cation gold complex encapsulated in the cage. This was built by positioning the vacuum optimized cation geometry in the capsule minimizing the root-mean-square-displacement (RMSD) with the X-ray structure of bis(trimethylphosphine) gold cation in $\text{Ga}_4\text{L}_6^{12-}$. The overall structure was further optimized with DFT. The starting geometry for the uncatalyzed reaction is the vacuum optimized gold complex. Both of these structures were then solvated using Gromacs with a pre-equilibrated water box of size 30Å x 30Å x 30Å for the encapsulated gold complex and 19Å x 19Å x 19Å for the reference reaction (without the cage). To maintain charge neutrality, potassium counter ions were also included at the positions provided in the X-ray resolved structure³² for the encapsulated system. We ran an additional 5ps *ab initio* molecular dynamics simulation (298K, 0.5 fs timestep) to further equilibrate the structures.

Ab initio metadynamics. Using these equilibrated solvated structures, we then ran well-tempered single walker metadynamics^{41, 42} as implemented in the CP2K package. To reduce the dimensions of the space to explore, we picked two collective variables that best describe the evolution of the reaction: (i) the distance between the carbon of the two leaving methyl groups and (ii) the coordination number (CN_{C-Au}) between the gold atom and the two carbons of the leaving methyl groups defined as follows:

$$CN_{C-Au} = \frac{1}{2} \sum_{i \in \{1,2\}} \frac{1 - \left(\frac{r_{Ci-Au}}{R_0}\right)^8}{1 - \left(\frac{r_{Ci-Au}}{R_0}\right)^{14}} \quad (2)$$

Where $r_{Ci-Au}(R_0)$ is the instantaneous (equilibrium) distance between the gold and carbon atoms. The choice of these coordinates was guided by our previous study for which we computed the geometry in vacuum of the reactant, transition state and product of the alkyl-alkyl reductive elimination reaction. It is also worth noting that, given the nature of the system, other candidates for collective variables (such as angles or dihedrals) would likely depend on either if not both the gold-methyl coordination number or the methyl-methyl distance.

In this metadynamics scheme, Gaussian functions of height 0.005 Ha were deposited at least every 30 steps (with a time step of 0.5 fs) along the trajectory in the reduced space. This introduces a history dependent bias that pushes the system towards areas of the landscape that would otherwise be hard to reach (such as the crossing between reactant and product wells). For both the catalyzed (with cage) and uncatalyzed (without cage) reactions, this process was run until the barrier was crossed at least 3 times, gathering over 50ps of metadynamics. Free energy surfaces were then created using the sub-program *graph* within the CP2K package. This tool reads in the information about the added Gaussian functions such as position, height and width and compute the corresponding unbiased energy landscape. From these, minimum energy paths were calculated using the zero temperature string method of Maragliano et al.⁴³ The procedure was performed in Matlab using a 30 point string and 3000 optimization steps.

To rationalize the role of the cage on the reduction of the reaction energy barrier, a set of geometries representative of the reactant and transition states were extracted. For the reactant state, we selected one structure every 10 fs of the molecular dynamics trajectory for 2 ps (200 structures total). For the transition state, we searched for a few snapshots within the metadynamics trajectory that corresponded to the values of the collective variables identified as

transition state by the string method. We then tested and refined our choice by performing a committer analysis until our selected geometries would fall in both the reactant and product equilibrium well. For the catalyzed reaction, we found 3 snapshots that displayed a 57% (43%) commitment to the product (reactant) state. These were situated at (2.1, 0.35) in the collective variable space, very close to the initial guess obtained by the string method (2.1, 0.36). Similarly, for the uncatalyzed reaction, we found 2 snapshots that displayed an early 38% (62%) commitment to the product (reactant) state, at (2.6, 0.24) in the collective variable space compared to the initial guess of (2.3, 0.24). An ensemble was then generated by gathering all geometries that fell within $\pm 0.05\text{\AA}$ in methyl-methyl distance and ± 0.005 in coordination number to (2.1, 0.35) for the catalyzed and (2.6, 0.24) for the uncatalyzed reaction. This represents about 45 geometries for each transition state ensemble for complete committer analysis statistics, thereby confirming that the transition state was reliably found.

Electric fields. The derivative of the electrostatic potential were obtained as direct output of CP2K, and the electric field was then projected onto the two bonds of the substrate that are most changed during the evolution of the reaction, namely the two gold-carbon of the leaving methyl group bonds (see Figure 5). The free energy state functions were obtained from this electric field projection through a model of the bond dipoles that were computed using the Density Derived Atomic Point Charge (DDAPC)⁴⁴ scheme that accounts for the multigrid integration of CP2K. The charges, bond lengths and details of these calculations are given in Supporting Information.

ACKNOWLEDGEMENTS

This work was supported by the Director, Office of Science, Office of Basic Energy Sciences, Chemical Sciences Division of the U.S. Department of Energy under Contract No. DE-10AC02-05CH11231. This research used resources of the National Energy Research Scientific Computing Center, a DOE Office of Science User Facility supported by the Office of Science of the U.S. Department of Energy under Contract No. DE-AC02-05CH11231.

Conflict of interest. The authors declare that they have no conflict of interest.

Author contribution. THG and VV conceived the scientific content and direction, V.V. and THG wrote the manuscript, and V.V. created the Figures and the table of contents image. Both authors contributed data and insights, discussed and edited the manuscript.

Data availability. The data that supports the findings of this study are available from the corresponding author upon request.

REFERENCES

1. Welborn VV, Ruiz Pestana L, Head-Gordon T. Computational optimization of electric fields for better catalysis design. *Nature Catal.* 2018, **1**(9): 649-655.
2. Vaissier Welborn V, Head-Gordon T. Computational Design of Synthetic Enzymes. *Chem. Rev.* 2019, **119**(11): 6613-6630.
3. Wiester MJ, Ulmann PA, Mirkin CA. Enzyme mimics based upon supramolecular coordination chemistry. *Angew. Chem. Int. Ed.* 2011, **50**(1): 114-137.
4. Meeuwissen J, Reek JN. Supramolecular catalysis beyond enzyme mimics. *Nature Chem.* 2010, **2**(8): 615-621.
5. Raynal M, Ballester P, Vidal-Ferran A, van Leeuwen PW. Supramolecular catalysis. Part 2: artificial enzyme mimics. *Chem. Soc. Rev.* 2014, **43**(5): 1734-1787.
6. Albada HB, Golub E, Willner I. Rational design of supramolecular hemin/G-quadruplex-dopamine aptamer nucleozyme systems with superior catalytic performance. *Chem. Sci.* 2016, **7**(5): 3092-3101.
7. Ballester P, Scarso A. Editorial: Supramolecular Aspects in Catalysis. *Front. Chem.* 2019, **7**: 174.
8. Wang QQ, Gonell S, Leenders SH, Durr M, Ivanovic-Burmazovic I, Reek JN. Self-assembled nanospheres with multiple endohedral binding sites pre-organize catalysts and substrates for highly efficient reactions. *Nature Chem.* 2016, **8**(3): 225-230.
9. Menger FM, Nome F. Interaction vs. Preorganization in Enzyme Catalysis. A Dispute that Calls for Resolution. *ACS Chem. Bio.* 2019, **14**(7): 1386-1392.
10. Brown CJ, Toste FD, Bergman RG, Raymond KN. Supramolecular catalysis in metal-ligand cluster hosts. *Chem. Rev.* 2015, **115**(9): 3012-3035.
11. Cullen W, Misuraca MC, Hunter CA, Williams NH, Ward MD. Highly efficient catalysis of the Kemp elimination in the cavity of a cubic coordination cage. *Nature Chem.* 2016, **8**(3): 231-236.
12. Welborn VV, Head-Gordon T. Fluctuations of Electric Fields in the Active Site of the Enzyme Ketosteroid Isomerase. *J. Am. Chem. Soc.* 2019, **141**(32): 12487-12492.
13. Zhang C, Shafi R, Lampel A, MacPherson D, Pappas CG, Narang V, *et al.* Switchable Hydrolase Based on Reversible Formation of Supramolecular Catalytic Site Using a Self-Assembling Peptide. *Angew. Chem. Int. Ed.* 2017, **56**(46): 14511-14515.
14. Ward MD, Hunter CA, Williams NH. Guest Binding and Catalysis in the Cavity of a Cubic Coordination Cage. *Chem. Lett.* 2017, **46**(1): 2-9.
15. Bhowmick A, Sharma SC, Head-Gordon T. The Importance of the Scaffold for de Novo Enzymes: A Case Study with Kemp Eliminase. *J. Am. Chem. Soc.* 2017, **139**(16): 5793-5800.

16. Zamfirescu C, Dincer I, Naterer GF. Analysis of a photochemical water splitting reactor with supramolecular catalysts and a proton exchange membrane. *Int. J. Hydrogen Energy* 2011, **36**(17): 11273-11281.
17. Ding X, Gao Y, Zhang L, Yu Z, Liu J, Sun L. Visible Light-Driven Water Splitting in Photoelectrochemical Cells with Supramolecular Catalysts on Photoanodes. *ACS Catal.* 2014, **4**(7): 2347-2350.
18. Hatano M, Sakamoto T, Mizuno T, Goto Y, Ishihara K. Chiral Supramolecular U-Shaped Catalysts Induce the Multiselective Diels-Alder Reaction of Propargyl Aldehyde. *J. Am. Chem. Soc.* 2018, **140**(47): 16253-16263.
19. Zhang Q, Catti L, Pleiss J, Tiefenbacher K. Terpene Cyclizations inside a Supramolecular Catalyst: Leaving-Group-Controlled Product Selectivity and Mechanistic Studies. *J. Am. Chem. Soc.* 2017, **139**(33): 11482-11492.
20. Nguyen NS, Das G, Yoon HH. Nickel/cobalt oxide-decorated 3D graphene nanocomposite electrode for enhanced electrochemical detection of urea. *Biosensors & bioelectronics* 2016, **77**: 372-377.
21. Jiang W, Wang X, Chen J, Liu Y, Han H, Ding Y, *et al.* Deuterohemin-Peptide Enzyme Mimic-Embedded Metal-Organic Frameworks through Biomimetic Mineralization with Efficient ATRP Catalytic Activity. *ACS Appl. Mat. & Inter.* 2017, **9**(32): 26948-26957.
22. French RR, Holzer P, Leuenberger MG, Woggon W-D. A Supramolecular Enzyme Mimic That Catalyzes the 15,15' Double Bond Scission of β -Carotene. *Angew. Chem. Int. Ed.* 2000, **39**(7): 1267-1269.
23. He Q, Kelliher M, Bahring S, Lynch VM, Sessler JL. A Bis-calix[4]pyrrole Enzyme Mimic That Constrains Two Oxoanions in Close Proximity. *J. Am. Chem. Soc.* 2017, **139**(21): 7140-7143.
24. Hong CM, Bergman RG, Raymond KN, Toste FD. Self-Assembled Tetrahedral Hosts as Supramolecular Catalysts. *Acc. Chem. Res.* 2018, **51**(10): 2447-2455.
25. Koblenz TS, Wassenaar J, Reek JN. Reactivity within a confined self-assembled nanospace. *Chem. Soc. Rev.* 2008, **37**(2): 247-262.
26. Nishioka Y, Yamaguchi T, Kawano M, Fujita M. Asymmetric [2 + 2] olefin cross photoaddition in a self-assembled host with remote chiral auxiliaries. *J. Am. Chem. Soc.* 2008, **130**(26): 8160-8161.
27. Tan C, Chu D, Tang X, Liu Y, Xuan W, Cui Y. Supramolecular Coordination Cages for Asymmetric Catalysis. *Chem.* 2019, **25**(3): 662-672.
28. Hong CM, Morimoto M, Kapustin EA, Alzakhem N, Bergman RG, Raymond KN, *et al.* Deconvoluting the Role of Charge in a Supramolecular Catalyst. *J. Am. Chem. Soc.* 2018, **140**(21): 6591-6595.
29. Kaphan DM, Toste FD, Bergman RG, Raymond KN. Enabling New Modes of Reactivity via Constrictive Binding in a Supramolecular-Assembly-Catalyzed Aza-Prins Cyclization. *J. Am. Chem. Soc.* 2015, **137**(29): 9202-9205.
30. Hart-Cooper WM, Sgarlata C, Perrin CL, Toste FD, Bergman RG, Raymond KN. Protein-like proton exchange in a synthetic host cavity. *Proc. Natl. Acad. Sci. USA* 2015, **112**(50): 15303-15307.
31. Hastings CJ, Pluth MD, Bergman RG, Raymond KN. Enzymelike catalysis of the Nazarov cyclization by supramolecular encapsulation. *J. Am. Chem. Soc.* 2010, **132**(20): 6938-6940.

32. Levin MD, Kaphan DM, Hong CM, Bergman RG, Raymond KN, Toste FD. Scope and Mechanism of Cooperativity at the Intersection of Organometallic and Supramolecular Catalysis. *J. Am. Chem. Soc.* 2016, **138**(30): 9682-9693.
33. Kaphan DM, Levin MD, Bergman RG, Raymond KN, Toste FD. A supramolecular microenvironment strategy for transition metal catalysis. *Science* 2015, **350**(6265): 1235-1238.
34. Hong CM, Kaphan DM, Bergman RG, Raymond KN, Toste FD. Conformational Selection as the Mechanism of Guest Binding in a Flexible Supramolecular Host. *J. Am. Chem. Soc.* 2017, **139**(23): 8013-8021.
35. Vaissier Welborn V, Head-Gordon T. Electrostatics Generated by a Supramolecular Capsule Stabilizes the Transition State for Carbon-Carbon Reductive Elimination from Gold(III) Complex. *J. Phys. Chem. Lett.* 2018, **9**(14): 3814-3818.
36. Mardirossian N, Head-Gordon M. Mapping the genome of meta-generalized gradient approximation density functionals: the search for B97M-V. *J. Chem. Phys.* 2015, **142**(7): 074111.
37. Mardirossian N, Head-Gordon M. Thirty years of density functional theory in computational chemistry: an overview and extensive assessment of 200 density functionals. *Mol. Phys.* 2017, **115**(19): 2315-2372.
38. VandeVondele J, Hutter J. Gaussian basis sets for accurate calculations on molecular systems in gas and condensed phases. *J. Chem. Phys.* 2007, **127**(11): 114105.
39. Hutter J, Iannuzzi M, Schiffmann F, VandeVondele J. cp2k: Atomistic simulations of condensed matter systems. *WIREs: Comp. Mol. Sci.* 2014, **4**(1): 15-25.
40. VandeVondele J, Krack M, Mohamed F, Parrinello M, Chassaing T, Hutter J. Quickstep: Fast and accurate density functional calculations using a mixed Gaussian and plane waves approach. *Comp. Phys. Comm.* 2005, **167**(2): 103-128.
41. Barducci A, Bussi G, Parrinello M. Well-tempered metadynamics: a smoothly converging and tunable free-energy method. *Phys. Rev. Lett.* 2008, **100**(2): 020603.
42. Barducci A, Bonomi M, Parrinello M. Metadynamics. *WIREs: Comp. Mol. Sci.* 2011, **1**(5): 826-843.
43. Maragliano L, Fischer A, Vanden-Eijnden E, Ciccotti G. String method in collective variables: minimum free energy paths and isocommittor surfaces. *J. Chem. Phys.* 2006, **125**(2): 24106.
44. Blöchl PE. Electrostatic decoupling of periodic images of plane-wave-expanded densities and derived atomic point charges. *J. Chem. Phys.* 1995, **103**(17): 7422-7428.